

Noisy homoclinic pulse dynamics

T. S. Eaves¹ and Neil J. Balmforth²

¹*Department of Applied Mathematics and Theoretical Physics, University of Cambridge, Cambridge, Wilberforce Road, CB3 0WA, UK*

²*Department of Mathematics, University of British Columbia, Vancouver, B.C. V6T 1Z2, Canada*

(Dated: 28 March 2016)

The effect of stochastic perturbations on nearly homoclinic pulse trains are considered for three model systems: a Duffing oscillator, the Lorenz-like Shimizu–Morioka model, and a co-dimension-three normal form. Using the Duffing model as an example, it is demonstrated that the main effect of noise does not originate from the neighbourhood of the fixed point, as is commonly assumed, but due to the perturbation of the trajectory outside that region. Singular perturbation theory is used to quantify this noise effect and applied to construct maps of pulse spacing for the Shimizu–Morioka and normal form models. The dynamics of these stochastic maps is then explored to examine how noise influences the sequence of bifurcations that take place adjacent to homoclinic connections in Lorenz-like and Shilnikov-type flows.

Keywords: homoclinic bifurcations, stochastic bifurcations, reduced models

Sequences of irregularly spaced pulses arise in a variety of nonlinear systems ranging from wavy fluid films and nerve axons to bursts in sheared convection and turbulent boundary layers. These solutions arise when the system is close to conditions under which there are homoclinic orbits connecting fixed points, and open analytical pathways to establishing key mathematical properties. Previously, these ideas have been exploited in deterministic systems to establish that strange attractors are possible in the form of trains of chaotically spaced pulses. Here, we extend the theory to stochastically perturbed systems. Along the way, we show how the main effect of noise is felt on the excursions away from the fixed points, rather than over the neighbourhood of those equilibria.

I. INTRODUCTION

Sequences of irregularly spaced pulses arise in a variety of deterministic nonlinear systems when conditions are close to those required for the homoclinic connection of a fixed point. Owing to the extended intervals that the system spends near the fixed point, the locally linear flow over the surrounding neighbourhood sensitively controls the dynamics. In tandem with simplifying assumptions for the relatively fast, nearly homoclinic or heteroclinic transitions away from the fixed points, significant mathematical progress is then possible to understand the dynamics and, in particular, show that attractors are possible with the form of trains of chaotically spaced pulses^{1,2}.

The notion that the flow in the vicinity of the fixed points controls the dynamics leads naturally to the expectation that this region acts as the clock that dictates the timings of a pulse train and any perturbation to the system should first be felt there. Stone & Holmes^{3,4} thereby

argued that stochastic perturbations of homoclinic (and heteroclinic) cycles take place near the fixed points and constructed a theory for how noise modified pulse timing (see also Ref. 5). In particular, they derived formulae for the mean pulse spacing of a stochastic Duffing equation and suggested how the pulse spacing distribution generically developed exponential tails. Further developments, including applications to other systems, can be found in Refs. 6 and 7.

Our goals in the current article are threefold. First, we show how the premise underlying Stone & Holmes’s analysis is, in fact, unfounded: the neighbourhood of the fixed points is not the critical region that controls the dynamics under stochastic perturbation. Instead, noise acting over the fast, near-homoclinic transitions significantly perturbs the location at which trajectories arrive at the origin. In turn, this produces variances in the timing of the pulses that are at least an order of magnitude larger than those due to noise near the origin.

To illustrate the point, we use the stochastic Duffing example of Stone & Holmes. The deterministic part of this example is

$$\dot{x} = y, \quad \dot{y} = x - x^3 - \gamma y + \beta x^2 y, \quad (1)$$

solutions of which are displayed in figure 1 for particular choices of the parameters β and γ . The fixed point at the origin is connected to itself by a homoclinic orbit for a special value of one of these parameters; we take $\gamma \equiv \gamma_*(\beta)$ to denote this special value. For $\gamma \approx \gamma_*$ but $\gamma > \gamma_*$, the homoclinic connection is slightly broken and a train of periodically spaced pulses arise. Owing to the symmetry of the system $(x, y) \rightarrow (-x, -y)$, for each homoclinic pulse there is also an “antipulse”, and when $\gamma \approx \gamma_*$ with $\gamma < \gamma_*$, there is an alternating sequence of pulses and antipulses.

Our second goal is to provide a formulation of the stochastically perturbed problem that accounts for the effect of noise away from the fixed points, and thereby enables us to predict the spacings of noisy pulse trains. For

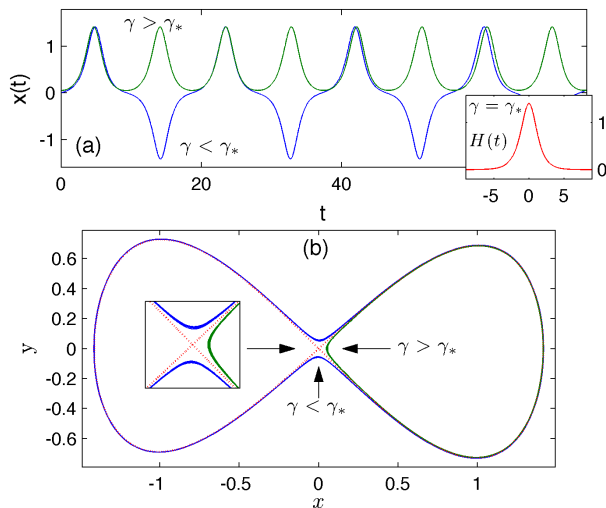


FIG. 1. The Duffing example in (1) with $\beta = 0.1$ and three values of γ : 0.079 ($< \gamma_*$), 0.081 ($> \gamma_*$) and 0.08001 ($\approx \gamma_*$). (a) shows time series of the three solutions and (b) a phase portrait on the (x, \dot{x}) plane.

the task, we use singular perturbation theory⁸, which was developed originally to describe the weak interactions of coherent structures in spatially extended systems⁹. One attractive feature of this method is that it immediately furnishes the timing map of a pulse train in terms of a number of integrals involving both the homoclinic orbit and a related adjoint function. This avoids the introduction of arbitrary constants in the linear mapping away from the fixed points which follow from the usual assumptions in the more geometrical approach of Shilnikov and others¹. That is, the theory is a predictive one, free of fitting constants.

The third goal is to use the methodology to study how stochastic perturbation affects bifurcations expected near homoclinic connections. These bifurcations depend sensitively on the nature of the stable and unstable manifolds of the fixed points. The so-called Lorenz flow² is typical when the dynamics near the fixed points is dominated by one-dimensional unstable and stable manifolds. The resulting second-order linear system is integral in connecting the overlapping tails of the monotonically growing and decaying pulses and helping to establish that systems like the Lorenz equations can possess a strange attractor. The union of unstable periodic orbits that comprise the attractor appear in a “homoclinic explosion”; further details of the bifurcation scenario are summarized in Ref. 2. An example of a Lorenz-like system is the Shimizu–Morioka model^{10–12}, given by

$$\dot{x} = y, \quad \dot{y} = x(1 - z) - \gamma y, \quad \dot{z} = \beta(x^2 - z), \quad (2)$$

as illustrated in figure 2 under nearly homoclinic conditions (for which, again, $\gamma = \gamma_*(\beta)$). For this example, there are again both pulses and antipulses and the solution now has chaotic spacings (for suitable saddle index).

When the flow near the fixed points is dominated by a one-dimensional unstable manifold and a two-dimensional stable manifold with complex eigenvalues, the homoclinic orbit trajectories grow monotonically, but decay in an oscillatory fashion. This leads to the Shilnikov bifurcation scenario in which a strange set of unstable periodic orbits can form through a complicated infinite sequence of period doubling cascades. The co-dimension-three normal form considered by Arneodo *et al.*¹³ provides a setting for the Shilnikov scenario and is defined by the system,

$$\ddot{x} + \gamma \ddot{x} + \dot{x} - \beta x + x^3 = 0. \quad (3)$$

We illustrate this third model in figure 3.

By adding noise to the two models in (2) and (3), we study how the homoclinic explosion of the Lorenz flow and Shilnikov’s bifurcation sequence are destroyed by noise. Our main tool is the spacing map furnished by the singular perturbation theory, which we verify provides a faithful first approximation of the dynamics of the stochastic differential systems. This extends to more complicated bifurcation scenarios earlier work on the effect of noise on single bifurcations and an isolated period doubling cascade^{14–16}. A preliminary report of this work¹⁷ contains additional results including some generalizations of the analysis of Stone & Holmes.

II. LOCATING THE NOISE EFFECT; THE STOCHASTIC DUFFING EQUATION

We add small noise terms to the system (1) to arrive at the stochastic ODEs,

$$\dot{x} = y + \varepsilon_x \xi_x(t), \quad (4)$$

$$\dot{y} = x - x^3 - \gamma y + \beta x^2 y + \varepsilon_y \xi_y(t), \quad (5)$$

where $(\varepsilon_x, \varepsilon_y) \ll 1$ parameterize the noise strengths and the precise form of the processes $\xi_x(t)$ and $\xi_y(t)$ will be prescribed presently.

In the vicinity of the origin, the deterministic system (1) can be linearized to show that this fixed point is a saddle with eigenvalues,

$$\lambda_{\pm} = \frac{1}{2}(-\gamma \pm \sqrt{\gamma^2 + 4}) \equiv \begin{cases} \lambda, \\ -\mu. \end{cases} \quad (6)$$

The coordinate axes can also be re-orientated so as to align them with the stable and unstable eigenvectors, which amounts to the linear transformation,

$$(x, y) \rightarrow (x_1, x_2), \quad x_1 = \frac{y - \lambda x}{\sqrt{1 + \lambda^2}} \quad x_2 = \frac{y + \mu x}{\sqrt{1 + \mu^2}}.$$

We may then define the local neighbourhood of the origin by \mathcal{D} , with $|x_1| \leq \delta$ and $|x_2| \leq \delta$ for some $\delta \ll 1$.

With reference to \mathcal{D} , we now prescribe the noise terms according to three specific scenarios:

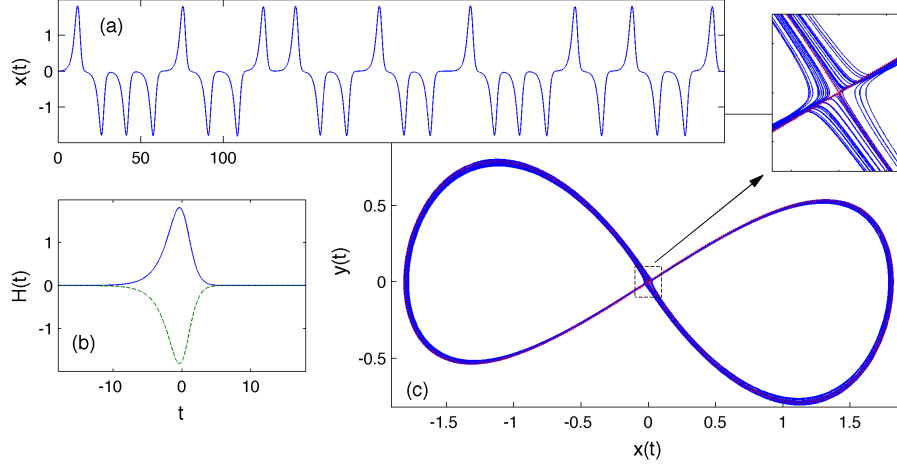


FIG. 2. The deterministic Shimizu–Morioka example in (2) with $\beta = 0.4$ and $\gamma = 1.19$. (a) shows time series of $x(t)$, (b) the homoclinic pulse and anti-pulse for $\gamma(\beta = 0.4) \approx 1.2054$, and (c) a portrait on the (x, y) plane. For the latter, a magnification of the neighbourhood of the origin is also overlaid and the homoclinic orbits are plotted (red lines).

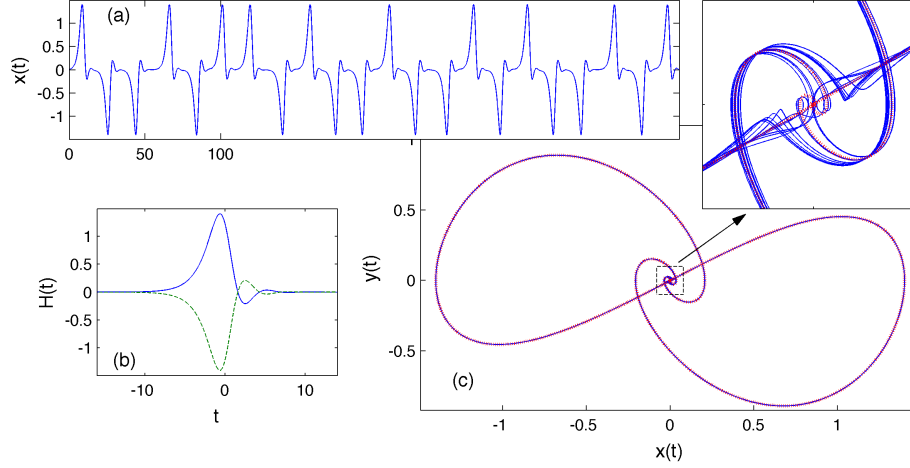


FIG. 3. The co-dimension-three normal form example in (3) with $\beta = 0.7$ and $\gamma = 1.108$. (a) shows time series of $x(t)$, (b) the homoclinic pulse and anti-pulse for $\gamma(\beta = 0.7) \approx 1.107887$, and (c) a portrait on the (x, y) plane. For the latter, a magnification of the neighbourhood of the origin is also overlaid and the homoclinic orbits are plotted (red lines).

- I. Noisy origin: $\xi_x = \xi_y = 0$ outside of \mathcal{D}
- II. Deterministic origin: $\xi_x = \xi_y = 0$ inside \mathcal{D}
- III. Noise everywhere: $(\xi_x, \xi_y) \neq 0$

Wherever the noise terms are not set to zero, we fix $\xi_x(t)$ and $\xi_y(t)$ to be independent realizations of the Gaussian white noise process $\xi(t)$ with

$$\mathbb{E}(\xi(t)) = 0, \quad \mathbb{E}(\xi(t)\xi(s)) = \delta(t - s). \quad (7)$$

For each scenario, we solve the stochastic ODEs numerically using a weak second-order scheme¹⁸ with a fixed time step of $\Delta t = 0.01$. The timings of the pulses and antipulses can then be extracted by finding the largest maxima of $|x(t)|$ over the times $t_n = n\Delta t$, $n = 0, 1, \dots$ (*i.e.* we avoid any interpolation within time steps); their differences furnish the pulse spacings $\Delta_n = t_n - t_{n-1}$.

Spacing distributions for the three scenarios I–III are displayed in figure 4 for the same choices of β and γ as in figure 1. Evidently, the spacing distributions for scenarios II and III are practically indistinguishable, with mean spacings $\langle \Delta \rangle \approx 10.2$. By contrast, scenario I is different, with a mean spacing of $\langle \Delta \rangle \approx 13.2$. Given that the stochastic perturbations reduce $\langle \Delta \rangle$, the higher mean spacing for scenario I suggests that the effective noise level is lower than in the other two scenarios. Another statistic of interest is the relative frequency for polarity reversal (the frequency at which a pulse switches to an antipulse, or *vice versa*). For the three scenarios this statistic is measured to be approximately 0.72, 0.51 and 0.52, all ± 0.01 , again confirming the equivalence of scenarios II and III, but not of I. In other words, adding noise everywhere is not equivalent to stochastically per-

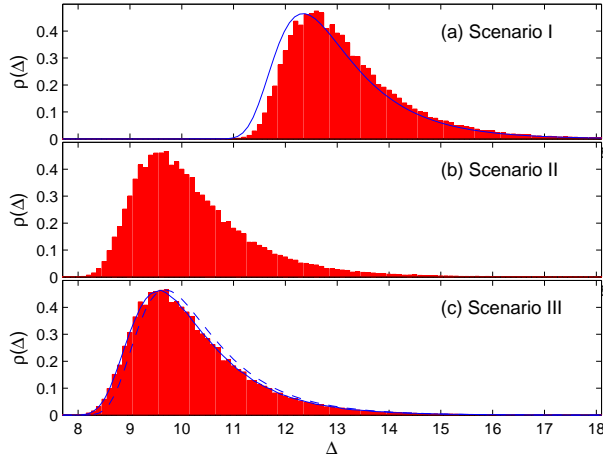


FIG. 4. Histograms of pulse spacings for the stochastic Duffing equation with $\varepsilon_x = \varepsilon_y = 0.0006$, $\beta = 0.1$ and $\gamma = 0.08$, for scenarios I–III. In (a), the red line shows the Stone-Holmes distribution in (10). In (c), the red line shows the distribution predicted by the asymptotic timing map in (29), and the dashed line shows the approximation (32).

turbing the dynamics in the vicinity of the origin.

Stone & Holmes assume that γ and β are relatively small and set $\varepsilon_x = \varepsilon_y = \varepsilon$ for the noise strengths. In this limit, $\lambda \approx \mu \approx 1$ and the homoclinic orbit is given by

$$H(t) = \sqrt{2} \operatorname{sech}(t), \quad (8)$$

which indicates that

$$T_R \approx 2 \log \left(\frac{4}{\delta} \right) \quad (9)$$

is the time-of-flight outside of \mathcal{D} (*i.e.* the time taken to proceed from $x \approx y \approx \delta/\sqrt{2}$ to $x \approx -y \approx \delta/\sqrt{2}$). For homoclinic conditions, Stone & Holmes then derive a form for the distribution of pulse spacings within \mathcal{D} ,

$$\rho(\Delta) = \frac{2\lambda\sqrt{\Lambda}e^{-\Lambda}}{\sqrt{\pi}(1-e^{-2\Lambda s})}, \quad \Lambda = \frac{\lambda\delta^2}{\varepsilon^2(e^{2\Lambda s}-1)}, \quad (10)$$

$$s = \Delta - T_R + \frac{1}{2\lambda} \ln \left(1 + \frac{\lambda}{\mu} \right),$$

which is compared with numerical data for scenario I in figure 4. For larger spacing, the factor $1 - e^{-2\Lambda s} \rightarrow 1$ in the denominator of $\rho(\Delta)$. It then follows that $Z = e^{-\lambda\Delta}$ is a Gaussian random variable with variance

$$\sigma_{SH}^2 = \frac{\delta\varepsilon}{16}; \quad (11)$$

up to a scaling, the variable Z corresponds to the coordinate at which the incoming trajectory intersects the border of \mathcal{D} .

Stone & Holmes continue on to establish that the mean pulse spacing is

$$\langle \Delta \rangle \sim T_R + \frac{1}{\lambda} \ln \left(\frac{\delta}{\varepsilon} \right) \operatorname{erf} \left(\frac{\delta}{\varepsilon} \sqrt{\mu} \right). \quad (12)$$

For $\delta\sqrt{\mu} \gg \varepsilon$, as in our example, this reduces to

$$\langle \Delta \rangle \sim 2 \log \left(\frac{4}{\delta} \right) + \frac{1}{\lambda} \log \left(\frac{\delta}{\varepsilon} \right) \sim \log \left(\frac{16}{\varepsilon\delta} \right), \quad (13)$$

which implies $\langle \Delta \rangle \sim 12.6$, and is close to the measured value of 13.2 for scenario I; computing the mean of (10) gives the somewhat better value of 13.0. Evidently, the theory of Stone & Holmes can be applied to scenario I. Notably, the mean spacing in (13) depends on δ , which has no significance in scenario III. The analysis with noise acting purely near the origin cannot therefore characterize the noise-everywhere case.

III. SPACING MAPS

A. Pulse-train asymptotics

To predict the timing between the pulses and antipulses of a noisy train, we add stochastic perturbations to the singular perturbation theory of Ref. 8. To pave the way, we first write our three model systems in the compact vectorial form,

$$\frac{d}{dt} \mathbf{x} = A\mathbf{x} + \mathbf{f}(\mathbf{x}) + \varepsilon\boldsymbol{\xi}, \quad (14)$$

where \mathbf{x} is the vector of dependent variables, A is a constant matrix, the nonlinear terms are represented by $\mathbf{f}(\mathbf{x})$, and $\varepsilon\boldsymbol{\xi}$ denotes the vector of noise terms.

The matrix A contains the parameter γ , which we adjust to be order $\varepsilon \ll 1$ close to the homoclinic value γ_* : $\gamma = \gamma_* + \varepsilon\gamma_1$. The small parameter ε therefore measures the breakage of the homoclinic connection in parameter space, and we assume that $\varepsilon = O(\varepsilon)$ so that stochastic perturbations are introduced at the same order. The adjustment of γ requires us to expand A as $A_0 + \varepsilon A_1$.

Let $\mathbf{H}(t) = (H^x, H^y)$ or (H^x, H^y, H^z) be the homoclinic pulse. Our model systems are reflection symmetric such that the antipulse is either $-\mathbf{H}(t)$ for the Duffing and normal-form cases, or $(-H^x, -H^y, H^z)$ for the Shimizu–Morioka model. To distinguish the pulses and antipulses, we therefore introduce the operation $\vartheta\mathbf{H} = \theta\mathbf{H}$ or $(\theta H^x, \theta H^y, H^z)$, defined using the polarity $\theta = \pm 1$.

We now look for a solution of the form,

$$\mathbf{x} = \sum_{k=-\infty}^{\infty} \mathbf{H}_k + \varepsilon\mathbf{R} + \dots, \quad (15)$$

where $\mathbf{H}_k = \vartheta_k \mathbf{H}(t - t_k)$ denotes a homoclinic solution centred at time t_k , and $\varepsilon\mathbf{R}$ denotes a remainder term which accounts for the fact that the overlap of neighbouring homoclinic orbits does not vanish and so the first sum in (15) is not an exact solution. However, we take the pulses to be well separated so that $\mathbf{H}_k \cdot \mathbf{H}_{k\pm 1} = O(\varepsilon)$. In other words, we consider the distinguished limit in which

the breakage of the homoclinic connection, the overlap of the pulses and the stochastic perturbation are all $O(\epsilon)$.

Substituting the ansatz (15) into (14) leads to a cancellation of the order-one terms in view of the equation satisfied by each \mathbf{H}_k . At the following order $O(\epsilon)$, in the vicinity of t_k , we obtain

$$\mathcal{L}_k \mathbf{R} = \frac{1}{\epsilon} \mathbf{J}(\mathbf{H}_k)(\mathbf{H}_{k+1} + \mathbf{H}_{k-1}) + A_1 \mathbf{H}_k + \frac{\epsilon}{\epsilon} \boldsymbol{\xi}, \quad (16)$$

where

$$\mathcal{L}_k = \frac{d}{dt} - A_0 - \mathbf{J}(\mathbf{H}_k), \quad (17)$$

and $J_{ij}(\mathbf{x}) = \partial f_i / \partial x_j$ is the Jacobian matrix of the non-linear function $\mathbf{f}(\mathbf{x})$. Note that the true operator acting on R involves the sum $\sum_k \mathbf{J}(\mathbf{H}_k)$, which includes all the pulses and antipulses. This sum is sharply peaked about each homoclinic trajectory, and so we may approximate the full operator by splitting up the sum and requiring R to satisfy a simpler equation for each k , incurring an error of higher order in ϵ .

The operator \mathcal{L}_k has adjoint

$$\mathcal{L}_k^\dagger = -\frac{d}{dt} - A_0^\dagger - \mathbf{J}(\mathbf{H}_k)^\dagger, \quad (18)$$

with null vector $\mathbf{N}_k \neq 0$ satisfying $\mathcal{L}_k^\dagger \mathbf{N}_k = 0$. The null vector again possesses a reflection symmetry for the three models. For the Duffing and normal-form examples, we take the null vector to be $\mathbf{N}_k = \vartheta_k \mathbf{N} = \theta_k \mathbf{N}(t - t_k)$ in terms of the k^{th} polarity and the null vector $\mathbf{N} = (N^x(t), N^y(t), N^z(t))$ of the homoclinic pulse. For Shimizu–Morioka model, we set $\mathbf{N}_k = \vartheta_k \mathbf{N} = (\theta_k N^x(t - t_k), \theta_k N^y(t - t_k), N^z(t - t_k))$.

Now we may take the dot product of (16) with \mathbf{N}_k and integrate to obtain

$$0 = \int_{-\infty}^{\infty} \mathbf{N}_k \cdot \left[\frac{1}{\epsilon} \mathbf{J}(\mathbf{H}_k)(\mathbf{H}_{k+1} + \mathbf{H}_{k-1}) + A_1 \mathbf{H}_k + \frac{\epsilon}{\epsilon} \boldsymbol{\xi} \right] dt. \quad (19)$$

With suitable changes of integration variable, and bearing in mind the dependences on polarity, the first two overlap terms on the right of (19) may be written more compactly in terms of pulse spacing, $\Delta_k = t_k - t_{k-1}$, and the integral function,

$$F_{k,l}(\Delta) = -\frac{1}{\epsilon} \int_{-\infty}^{\infty} \vartheta_k \mathbf{N}(t) \cdot \mathbf{J}(\vartheta_k \mathbf{H}(t)) \vartheta_l \mathbf{H}(t + \Delta) dt. \quad (20)$$

In particular, we may write the spacing map,

$$F_{k,k+1}(-\Delta_{k+1}) = c + m\eta_k - F_{k,k-1}(\Delta_k), \quad (21)$$

where

$$c = \int_{-\infty}^{\infty} \mathbf{N}(t) \cdot A_1 \mathbf{H}(t) dt \quad (22)$$

and the noise term is written as the product of a Gaussian random variable η_k with zero mean and unit variance, and an amplitude m given by

$$m^2 = \int_{-\infty}^{\infty} \sum_{j=1}^{\ell} \left[\frac{\epsilon_j}{\epsilon} N^j(t) \right]^2 dt, \quad (23)$$

where $\ell = 2$ or 3 is the order of each model. Note that (21) determines both the spacing and polarity of the next pulse according to the size and sign of the combination, $c + m\eta_k - F_{k,k-1}(\Delta_k)$, respectively. Moreover, the introduction of a new variable, $Z_{k+1} = F_{k,k+1}(-\Delta_{k+1})$, turns (21) into a more obvious one-dimensional map with additive noise.

B. Revisiting Duffing

For the Duffing equation we may write $(H^x, H^y) = (H, \dot{H})$ and $(N^x, N^y) = (\dot{N}, N)$. The spacing function and detuning constant in (19) and (22) can then be written in the more transparent forms,

$$F_{k,l}(\Delta) = \frac{1}{\epsilon} \theta_k \theta_l \int_{-\infty}^{\infty} [3N(t) + \beta \dot{N}(t)] H^2(t) H(t + \Delta) dt \quad (24)$$

and

$$c = -\gamma_1 \int_{-\infty}^{\infty} N(t) \dot{H}(t) dt. \quad (25)$$

Provided the pulses are well spaced, we may further reduce $F_{k,l}(\Delta)$ using the tails of the homoclinic orbit:

$$\begin{aligned} H(t + \Delta_k) &\sim h_\infty e^{-\mu(t + \Delta_k)} \\ H(t - \Delta_{k+1}) &\sim h_0 e^{\lambda(t - \Delta_{k+1})}. \end{aligned} \quad (26)$$

Hence

$$\begin{aligned} F_{k,k+1}(-\Delta_{k+1}) &\sim \frac{h_0}{\epsilon} \Theta_{k+1} e^{-\lambda \Delta_{k+1}} \int_{-\infty}^{\infty} (3N + \beta \dot{N}) H^2 e^{\lambda t} dt \\ &\equiv \frac{A}{\epsilon} \Theta_{k+1} e^{-\lambda \Delta_{k+1}}, \end{aligned} \quad (27)$$

and

$$\begin{aligned} F_{k,k-1}(\Delta_k) &\sim \frac{h_\infty}{\epsilon} \Theta_k e^{-\mu \Delta_k} \int_{-\infty}^{\infty} (3N + \beta \dot{N}) H^2 e^{-\mu t} dt \\ &\equiv \frac{B}{\epsilon} \Theta_k e^{-\mu \Delta_k}, \end{aligned} \quad (28)$$

where the relative polarity is $\Theta_k = \theta_k \theta_{k-1}$. We are then left with the timing map

$$\Theta_{k+1} e^{-\lambda \Delta_{k+1}} = C + \Theta_k D e^{-\mu \Delta_k} + \sigma \eta_k, \quad (29)$$

where $C = \epsilon c / A$, $D = -B / A$ and $\sigma = \epsilon m / |A|$.

When γ and β are small, the limiting analytical form of the homoclinic pulse in (8) along with $N = \dot{H}$ imply

$C \rightarrow \epsilon\gamma_1/12$, $D \rightarrow 1$ and $\sigma \rightarrow (\epsilon_y^2/3 + 7\epsilon_x^2/15)^{1/2}/8$. For the numerical example provided in section 2, these constants turn out to be $C = -1.3621 \times 10^{-6}$, $D \approx 1.3767$ and $\sigma \approx 7.8532 \times 10^{-5}$. The resulting spacing map is illustrated in figure 5, and is double-valued owing to polarity reversals¹⁹. Sample iterations with added noise are also included in the figure, and scatter increasingly far from the deterministic map on raising the noise level. The spacing distribution determined by iterating the resulting map a million times also shows satisfying agreement with that measured from solving the stochastic ODE (see figure 4(c); the mean pulse spacing from the map is $\langle \Delta \rangle \approx 10.2$).

We can convert (29) into the more conventional looking one-dimensional map,

$$Z_{k+1} = C + \text{sgn}(Z_k)D|Z_k|^{\mu/\lambda} + \sigma\eta_k. \quad (30)$$

where $Z_k = \Theta_k e^{-\lambda\Delta_k}$ is equivalent to a scaled coordinate on a Poincaré section at the border of the neighbourhood of the origin, as in §II. The breakage of the homoclinic connection is measured by C . The second term on the right of (30) represents the effect of the previous close passage by the origin. The final noise term is additive, has an amplitude set by $\sigma = O(\epsilon)$, and corresponds to the uncertainty in the location where the trajectory re-enters the origin's vicinity due to stochastic perturbation of the nearly homoclinic pulse. In Stone & Holmes's analysis, noise near the origin generates uncertainty in the residence time there, equivalent to a stochastic perturbation of the second term on the right of (30). The corresponding amplitude, σ_{SH} in (11), is $O(\delta\epsilon)$, which is $O(\delta) \ll 1$ smaller than the noise term in (30). This rationalizes our observation that scenarios II and III are equivalent, but scenario I is different and effectively less noisy.

Given that $\mu > \lambda$, the map (30) has a stable deterministic fixed point $Z_k = Z_* = O(\epsilon)$. When the noise level is relatively low, one then expects an approximate stationary distribution for Z_k given by²⁰

$$\rho_Z(Z) = \frac{1}{\sqrt{2\pi}\Sigma^2} \exp\left[-\frac{(Z - Z_*)^2}{2\Sigma^2}\right], \quad (31)$$

where $\Sigma = \sigma/\sqrt{1 - [f'(Z_*)]^2}$ and $|f'(Z)| = \mu|Z|^{\mu/\lambda-1}/\lambda$. The corresponding spacing distribution is

$$\rho_\Delta(\Delta) = \frac{\lambda e^{-\lambda\Delta}}{\sqrt{2\pi}\Sigma^2} \left\{ \exp\left[-\frac{(e^{-\lambda\Delta} - Z_*)^2}{2\Sigma^2}\right] + \exp\left[-\frac{(e^{-\lambda\Delta} + Z_*)^2}{2\Sigma^2}\right] \right\}, \quad (32)$$

which is also drawn in figure 4(c). From $\rho_\Delta(\Delta)$, we may estimate the mean pulse spacing:

$$\langle \Delta \rangle = \int_0^\infty \Delta \rho_\Delta(\Delta) d\Delta \sim \begin{cases} \lambda^{-1} \log(Z_*^{-1}), & \Sigma \ll |Z_*|, \\ \lambda^{-1} \log(\Sigma^{-1}) + \frac{1}{2}\lambda^{-1}(\gamma_e + \log 2), & |Z_*| \ll \Sigma, \end{cases} \quad (33)$$

where γ_e is Euler's gamma constant. The two limits here correspond to the deterministic spacing value at the fixed

point and the noise-driven spacing under homoclinic conditions. The latter gives the leading-order estimate

$$\langle \Delta \rangle \sim \lambda^{-1} \log(\Sigma^{-1}) \rightarrow \frac{1}{2} \log\left(\frac{192}{\epsilon_y^2 + 7\epsilon_x^2/5}\right) \quad (34)$$

for small γ and β , providing a counterpart to Stone & Holmes's prediction in (13). Figure 5(b) plots mean pulse spacing against noise level $\epsilon = \epsilon_y$ with $\epsilon_x = 0$, for both numerical solutions of the stochastic ODEs and iterations of the spacing map; the agreement is again satisfying. Both sets of data converge to the limits in (33) for relatively low and high noise levels, at least until the weak-noise approximation underlying (32) fails for $\epsilon > 10^{-3}$.

For the value of γ in figures 4 and 5, a periodic train of pulses and antipulses emerges without noise ($\gamma < \gamma_*$). The relative frequency for polarity reversal, $\frac{1}{2}(1 - \langle \Theta \rangle)$, is therefore one. As the deterministic dynamics becomes washed out by noise, on the other hand, the polarity reverses on average every other excursion away from the origin, and so $\frac{1}{2}(1 - \langle \Theta \rangle) \rightarrow \frac{1}{2}$. The passage between these two limits is illustrated in figure 5(c). The progression of the mean spacing and polarity reversal frequency as γ passes through its homoclinic value is shown in figure 5(d) and (e) for different levels of noise; the noise limits the mean spacings reached for $\gamma \rightarrow \gamma_*$ and smooths out the switch from $\frac{1}{2}(1 - \langle \Theta \rangle) = 1$ to 0. All the while, there is agreement between the results from the map and stochastic ODEs.

IV. NOISY LORENZ MAPS; THE STOCHASTIC SHIMIZU-MORIOKA MODEL

For the Shimizu-Morioka model, the eigenvalues at the origin are

$$-\beta, \quad -\frac{1}{2}(-\gamma - \sqrt{4 + \gamma^2}) \quad \text{and} \quad \lambda = \frac{1}{2}(\sqrt{4 + \gamma^2} - \gamma). \quad (35)$$

We consider the case $\frac{1}{2}(-\gamma - \sqrt{4 + \gamma^2}) > \beta$, and so the homoclinic orbit therefore has the leading-order tails,

$$\begin{aligned} \mathbf{H} &\sim (h_0^x, h_0^y, 0) e^{\lambda t} \quad \text{as } t \rightarrow -\infty \\ \mathbf{H} &\sim (0, 0, h_\infty^z) e^{-\beta t} \quad \text{as } t \rightarrow \infty \end{aligned} \quad (36)$$

(omitting the other stable eigenvalue is equivalent to assuming that strong contraction in the corresponding direction renders trajectories essentially two-dimensional when passing near the origin; cf. figure 2). Thence,

$$F_{k,k-1}(\Delta_k) \sim \frac{h_\infty^z}{\epsilon} e^{-\beta\Delta_k} \int_{-\infty}^{\infty} H^x N^y e^{-\beta t} dt \equiv \frac{B}{\epsilon} e^{-\beta\Delta_k} \quad (37)$$

and

$$\begin{aligned} F_{k,k+1}(-\Delta_{k+1}) &\sim \frac{h_0^x}{\epsilon} \Theta_{k+1} e^{-\lambda\Delta_{k+1}} \int_{-\infty}^{\infty} (H^z N^y - 2\beta H^x N^z) e^{\lambda t} dt \\ &\equiv -\frac{A}{\epsilon} e^{-\lambda\Delta_{k+1}} \Theta_{k+1}, \end{aligned} \quad (38)$$

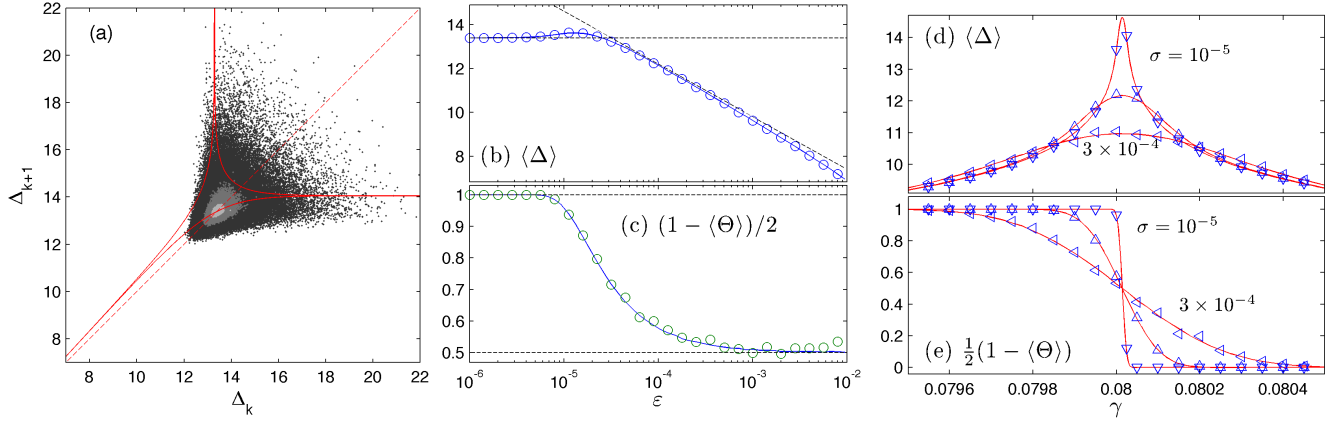


FIG. 5. (a) The deterministic spacing map of the Duffing equation for $\gamma = 0.08$ and $\beta = 0.1$ (red curves); the dashed line is the diagonal. The points show iterations of the noisy map with $\sigma = 10^{-5}$, 3×10^{-6} and 10^{-6} (with the grey shading increasing with σ). (b) and (c) show how the mean pulse spacing, $\langle \Delta \rangle$, and frequency of polarity reversal, $(1 - \langle \Theta \rangle)/2$, vary with noise level ε for numerical computations of the stochastic ODEs (circles) and from iterations of the map (solid lines). The dashed lines show the asymptotes in (33) for (b), and the limits $\frac{1}{2}$ and 1 in (c). (d) and (e) plot mean spacings and reversal frequencies against γ for $\sigma = 10^{-5}$, 10^{-4} and 3×10^{-4} ; solid lines show results from the map, and triangles from the stochastic ODEs.

which furnish the spacing map,

$$\Theta_{k+1}e^{-\lambda\Delta_{k+1}} = C + De^{-\beta\Delta_k} + \sigma\eta_k, \quad (39)$$

where

$$C = \epsilon\gamma_1 A^{-1} \int_{-\infty}^{\infty} N^y H^y dt. \quad (40)$$

Here, again, η_k is a Gaussian random variable with zero mean and unit variance, the noise strength is $\sigma = \epsilon m/|A|$ and $D = B/A$, but with the different definitions of A and B implicit in (37) and (38).

The (single-valued) spacing map in (39) is illustrated in figure 6 for the parameter settings of figure 2. Panel (a) compares the deterministic map with spacing data extracted from a numerical solution of the ODEs. For this example, the agreement between the two is less satisfactory than for the Duffing example, primarily because the proximity to homoclinicity is less well tuned (the pulses are less separated) and because we neglect the second stable eigenvalue in constructing the map.

Note that the iterates from the ODE only superficially form a one-dimensional map; fractal structure is hidden in the finer details of the spacing plot⁸. This is familiar from the Lorenz system, where the return maps from Poincaré sections conceal fractal structure². Indeed, by defining $Z_k = \Theta_k \exp(-\lambda\Delta_k)$, we may turn the spacing map into the more standard form

$$Z_{k+1} = C + \text{sgn}(Z_k)B|Z_k|^{\beta/\lambda} + \sigma\eta_k, \quad (41)$$

which, without the noise term, is equivalent to the return map used to illustrate the Lorenz bifurcation sequence.

To illustrate the effect of noise, we set $\varepsilon_x = \varepsilon_y = \varepsilon_z = \varepsilon$. As displayed in the second panel in figure 6, noise smears out the spacing iterations around the curve of

the deterministic map and shortens the lowest spacings sampled by the train (panel (b)). Simultaneously, the noise smooths out any structure in the spacing distribution (panels (c) and (d)), which have exponential tails, both with and without noise (*cf.* Ref. 4). As shown in panels (d) and (e), noise lowers both the mean spacing and frequency of polarity reversal, although the comparison of the results from the map and stochastic ODEs is again less satisfactory.

The deterministic part of the spacing map (41) (setting $\sigma = 0$) captures the bifurcations to chaos that characterize nearly homoclinic Lorenz flow (provided the “saddle index” $\beta/\lambda < 1$): at $C = 0$, an infinite number of unstable periodic orbits appear in a homoclinic explosion. This set does not immediately form a strange attractor, however, because the set is contained within the basin of attraction of a coexisting stable fixed point. As C is decreased below zero, the set moves out of the basin of attraction at a boundary crisis, to turn into a strange attractor. At a sufficiently negative value of C , the stable fixed point disappears in a saddle node, leaving the strange set as the only attractor. These three bifurcations are all familiar from the Lorenz equations², and their impact on the map structure is illustrated in the sequence shown in figure 7. Also shown is a bifurcation diagram plotting spacing iterations from the map against the homoclinity parameter C , together with all the unstable fixed points and period-2, 3 and 4 orbits (some of which disappear at smaller C in secondary homoclinic bifurcations). Between the saddle-node and crisis, both the stable fixed point and strange attractor co-exist, and the system is hysteretic if C is raised or lowered through this interval.

The effect of adding noise to the map on the bifurcation diagram is shown in figure 8. The noise widens and

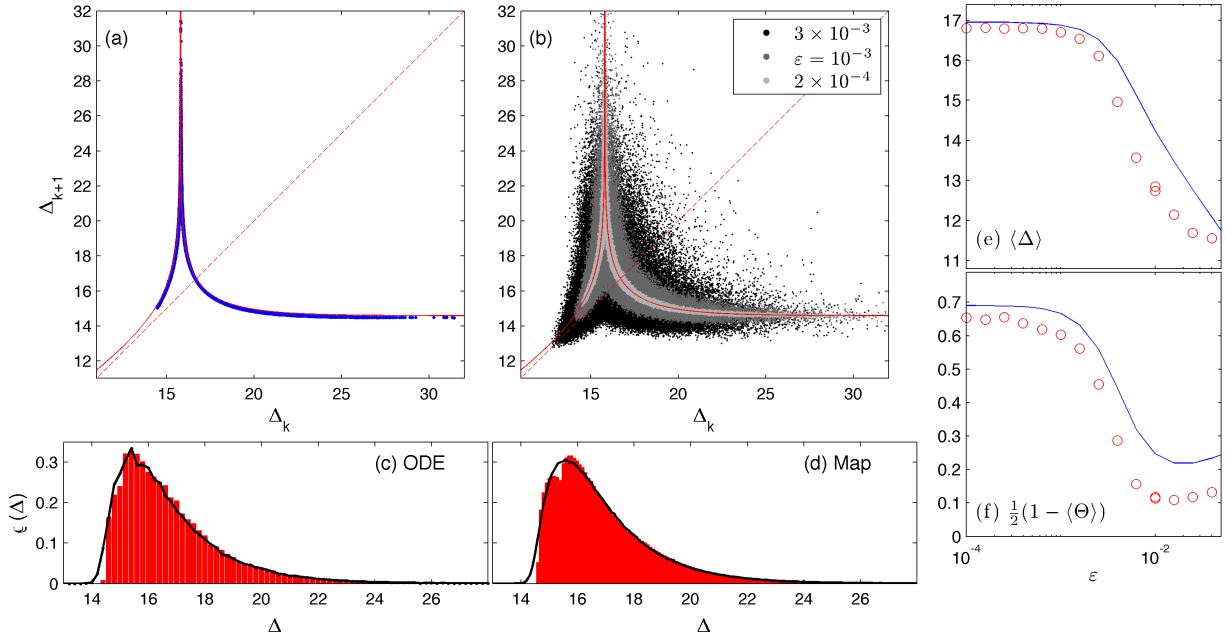


FIG. 6. Spacing map for the Shimizu–Morioka system with $\gamma = 1.19$ and $\beta = 0.4$. In (a) the spacing map (solid line) is compared with timing data extracted from a solution to the stochastic ODEs (points); the dashed line shows the diagonal. In (b), the spacing map is redrawn, and iterates of the noisy map are added with $\varepsilon = 2 \times 10^{-4}$, 10^{-3} and 3×10^{-3} (points, with grey shading increasing with ε). Underneath we show spacing distributions computed using (c) the stochastic ODEs and (d) the spacing map. The histograms indicate the deterministic case; the lines represent noisy cases with $\varepsilon = 10^{-3}$. (d) and (e) show the mean spacing and polarity reversal frequency against noise level; the solid lines show results from the map, the circles from the stochastic ODEs.

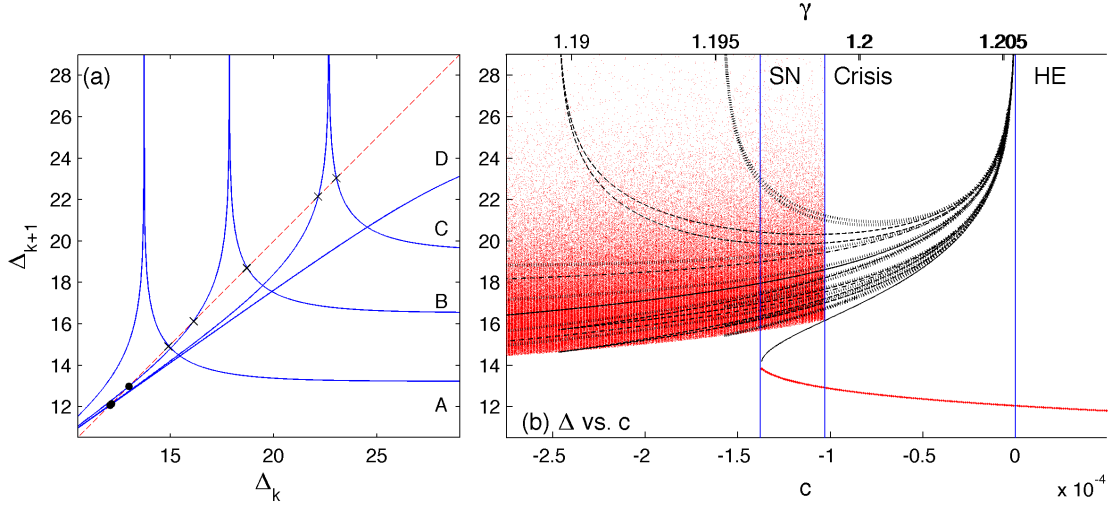


FIG. 7. (a) A sequence of spacing maps for $\gamma = 1.17$ (A), 1.1986 (B), 1.2044 (C) and 1.2054 (D), showing the change in structure due the homoclinic explosion (HE), crisis of the strange attractor and the saddle node (SN); stable fixed points are plotted at dots, unstable ones as crosses. (b) a bifurcation diagram showing spacing against homoclinicity parameter C . Red dots indicate map iterations with transients removed, obtained by both raising and lowering C . The black lines show the unstable fixed points (solid), and period-2 (dot-dashed), period-3 (dashed) and period-4 (dotted) orbits.

smooths the spacing distributions around the stable fixed point and strange attractor. More importantly, however, it enables iterations to escape from the chaotic attractor for some of the parameter settings for which the two at-

tractors co-exist deterministically, narrowing the window of C (and the number of iterations) for which hysteresis can be observed. For sufficiently strong noise, the hysteresis of the deterministic system becomes completely

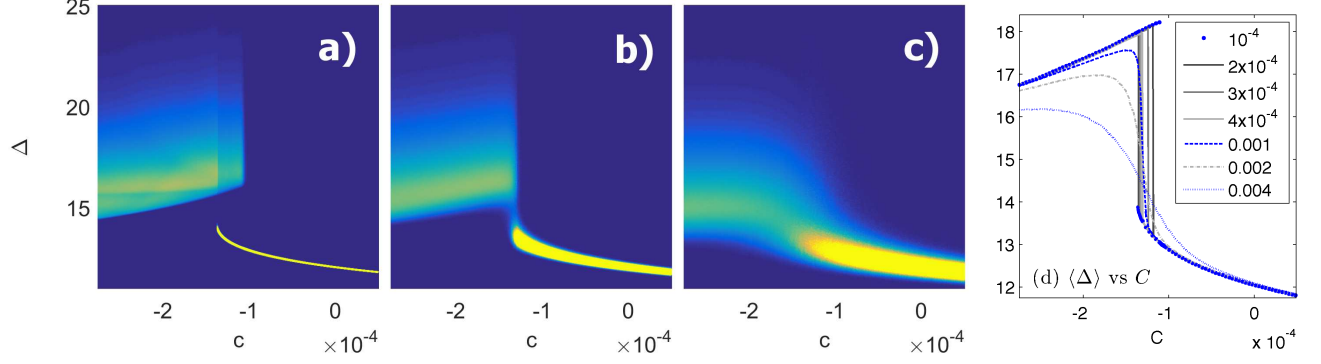


FIG. 8. Noisy bifurcation diagrams of spacing against C for (a) $\varepsilon = 10^{-4}$, (b) 10^{-3} and (c) 4×10^{-3} , with $\beta = 0.4$. In each case a fixed number of map iterations (with transients removed) are turned into a density on the (C, Δ) -plane. The corresponding mean spacings are shown in (d), together with additional results for more values of ε (as indicated).

lost, with the broad peak in spacing density adjusting sharply in the vicinity of the saddle node from the relic of the strange set to the noisy stable fixed point.

V. A STOCHASTIC SHILNIKOV SYSTEM

The normal-form model has a saddle at the origin with a one-dimensional unstable direction and a two-dimensional stable manifold in which the dynamics is a focus. We may write $(H^x, H^y, H^z) = (H, \dot{H}, \ddot{H})$ and $(N^x, N^y, N^z) = (\ddot{N}, \dot{N}, N)$. For the homoclinic orbit,

$$H \sim \begin{cases} h_0 e^{\lambda t} & \text{as } t \rightarrow -\infty, \\ h_\infty e^{-\mu t} \cos(\omega t + \phi) & \text{as } t \rightarrow \infty, \end{cases} \quad (42)$$

where $-\mu \pm i\omega$ denotes the complex stable eigenvalue, for some h_0 , h_∞ and ϕ . With these tails for $H(t)$, we find

$$\begin{aligned} F_{k,k+1}(-\Delta_{k+1}) &\sim \frac{3}{\epsilon} h_0 \Theta_{k+1} e^{-\lambda \Delta_{k+1}} \int_{-\infty}^{\infty} N H^2 e^{\lambda t} dt \\ &\equiv \frac{A}{\epsilon} e^{-\lambda \Delta_{k+1}} \Theta_{k+1} \end{aligned} \quad (43)$$

and

$$\begin{aligned} F_{k,k-1}(\Delta_k) &\sim \frac{3}{\epsilon} h_\infty \Theta_k e^{-\mu \Delta_k} \int_{-\infty}^{\infty} N H^2 e^{-\mu t} \cos[\omega(t + \Delta_k) + \phi] dt \\ &\equiv \frac{B}{\epsilon} e^{-\mu \Delta_k} \Theta_k \cos(\omega \Delta_k + \Phi). \end{aligned} \quad (44)$$

The spacing map is then

$$\Theta_{k+1} e^{-\lambda \Delta_{k+1}} = C + \Theta_k D e^{-\mu \Delta_k} \cos(\omega \Delta_k + \Phi) + \sigma \eta_k, \quad (45)$$

where $D = -B/A$, A and B are now defined by (43)–(44), the noise term is written as for the other two models, and

$$C = \epsilon \gamma_1 A^{-1} \int_{-\infty}^{\infty} N H dt, \quad (46)$$

The map (45) was written down previously without any derivation by Arecchi *et al.*²¹.

The deterministic spacing map is illustrated in figure 9 and compared with spacing iterations from corresponding numerical solutions of the ODE. The map is rendered double-valued by polarity replication or reversal, and fractal structure is concealed in the finer details of the ODE data⁸. The iterates of the map and ODE agree to within the thickness of the plotted curves and points (the mean spacing of both is $\langle \Delta \rangle \approx 17.8$; the polarity reversal frequency is $(1 - \langle \Theta \rangle)/2 = 0.74 \pm 0.01$ for the ODE, and 0.73 ± 0.01 for the map).

We illustrate the effect of noise by taking $\varepsilon_z = \varepsilon$ and $\varepsilon_x = \varepsilon_y = 0$. Figure 9 includes a weakly noisy solution of the ODE for $\varepsilon = 10^{-6}$; the spacing iterations spread slightly about the deterministic map. Despite this mild effect, the spacing distribution is significantly smoothed by the addition of this low level noise. For $\varepsilon = 0$, the spacing distribution is a highly structured invariant measure that is awkward to compare between map and ODE. The agreement between the noisy distributions with $\varepsilon = 10^{-6}$ is, however, satisfying (see panel (b)), as is the comparison of mean spacing and polarity reversal frequency for varying noise level (panels (c)–d)).

The influence of stronger levels of noise is illustrated using the map in figure 10. The most significant effect is chiefly at larger spacing for weaker noise levels (in terms of the spread of expected spacing about the deterministic map). The effect amplifies and spreads to shorter spacings as the noise level is raised. The noise also prompts sudden expansions in the spacing distribution (noise-induced boundary crises²²), when fluctuations repeatedly drive iterations beyond fixed points at smaller spacing, exposing additional loops in the curve of the map (corresponding to fewer turns around the origin in the Shilnikov flow). Such expansions eventually lead to a breakdown of the map once spacings are reduced sufficiently that the pulses are no longer widely spaced.

Bifurcation diagrams for the spacing map are shown in figure 11. Such diagrams are intricate owing to the

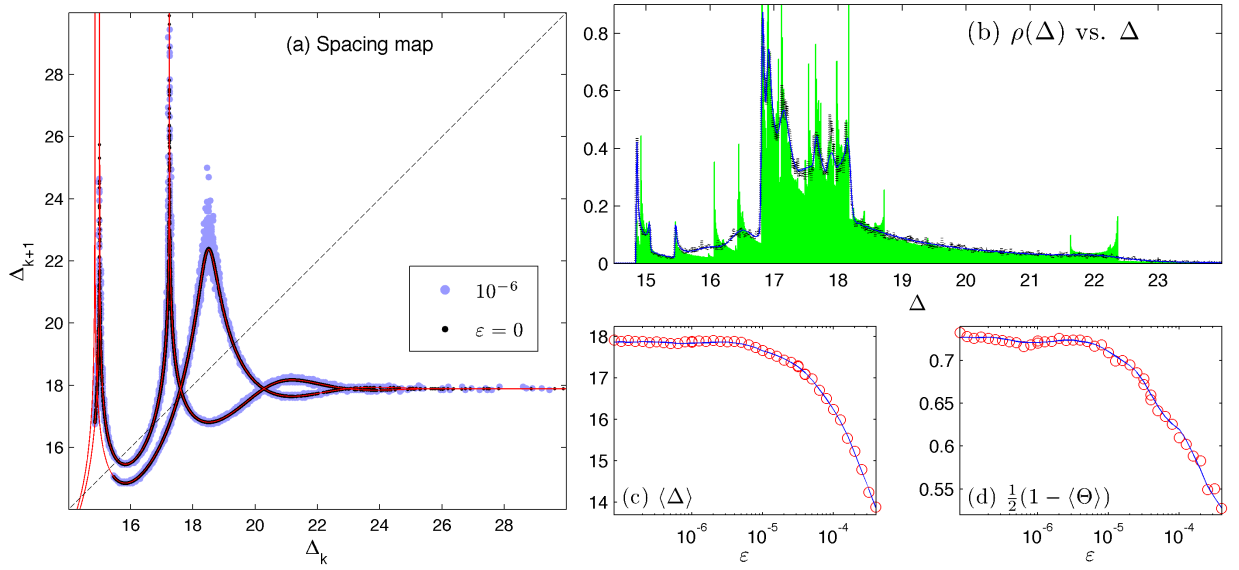


FIG. 9. (a) Spacing map (45) for $\gamma = 1.108$ and $\beta = 0.7$. The red lines show the double-valued deterministic map (45) and the dashed line is the diagonal. The dark and light (blue) points show 15000 pulse spacings extracted from numerical solutions of the ODE with noise levels of $\varepsilon = 0$ and 10^{-6} . (b) the distribution of pulse spacings from the ODE for $\varepsilon = 10^{-6}$ (dotted line), and from the map for $\varepsilon = 0$ (light green histogram) and 10^{-6} (solid line). Panels (c) and (d) plot the mean spacing and polarity reversal frequency against noise level.

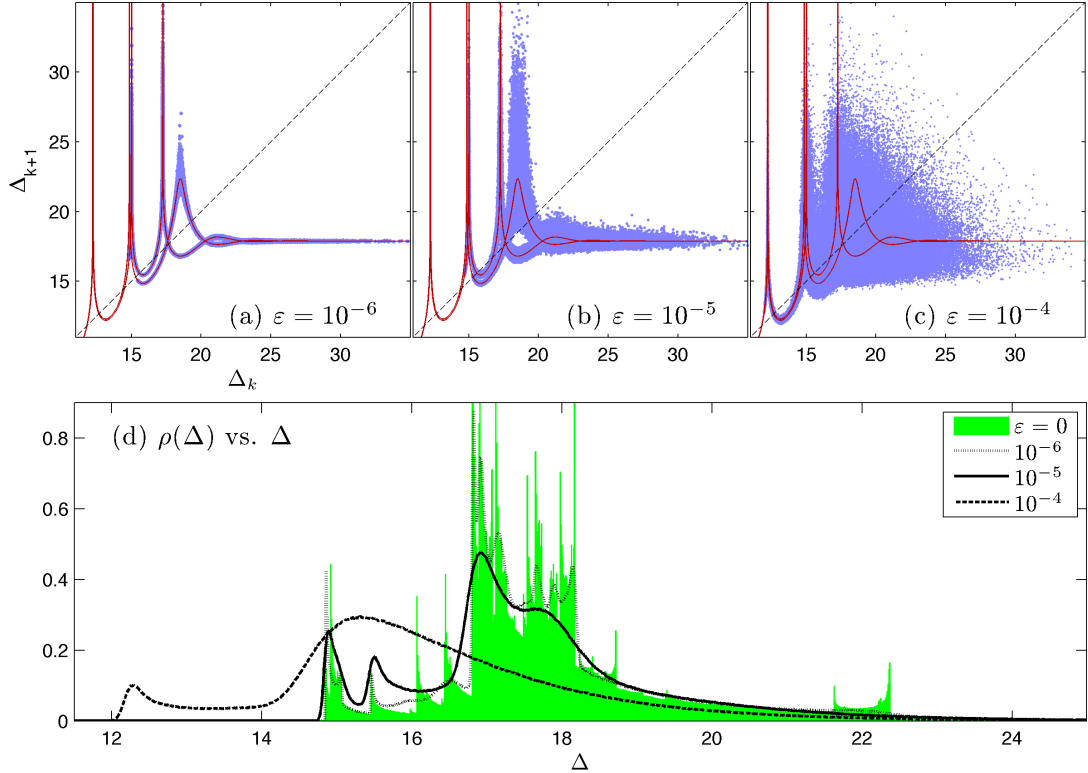


FIG. 10. Noisy Shilnikov maps for (a) $\varepsilon = 10^{-6}$, (b) $\varepsilon = 10^{-5}$ and (c) $\varepsilon = 10^{-4}$ ($\gamma = 1.108$, $\beta = 0.7$). The solid (red) lines show the double-valued deterministic map and the dashed line is the diagonal. Panel (d) shows spacing distributions for the same noise levels; the light (green) histogram shows the deterministic invariant measure.

fixed point that winds up to infinite period and the associated period-doubling cascades^{1,23}. For the cur-

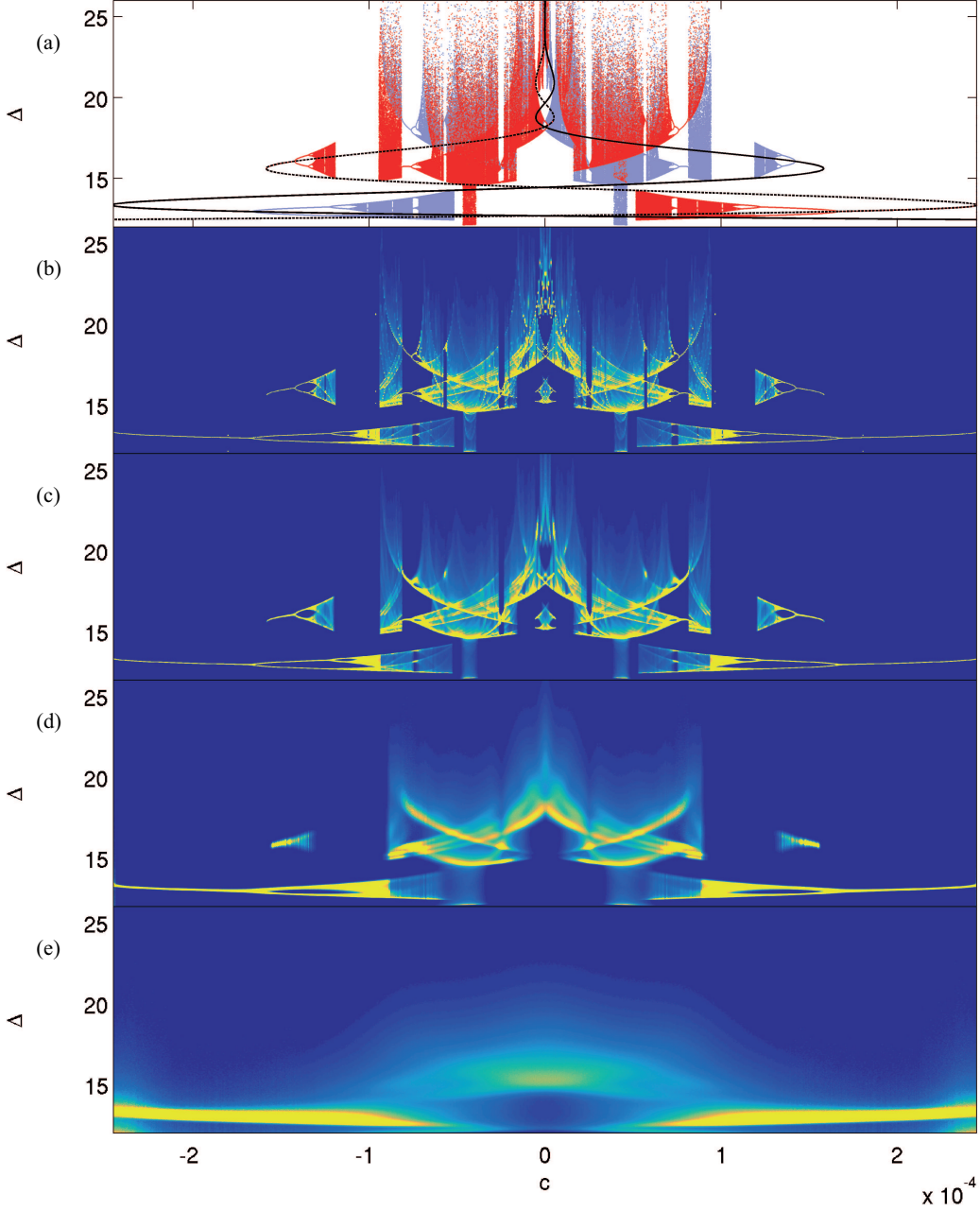


FIG. 11. Bifurcation diagrams for Shilnikov spacing maps. (a) plots fixed points and iterations of the deterministic map against C , with polarity replication (reversals) spacings shown as solid (dashed) lines and blue (red) points. Transients are removed for the iterations. (b)–(e) show iterations of the noisy map with $\varepsilon = 10^{-7}$, 10^{-6} , 10^{-5} and 10^{-4} , collected as densities on the (C, Δ) –plane.

rent map, the situation is made yet more convoluted by the pulse-antipulse symmetry, which introduces a second fixed point and set of cascades that appear as a mirror image in the bifurcation diagram²⁴. The first panel of figure 11 focusses on a part of the bifurcation diagram for the deterministic map; the loci of the two winding fixed points are visible along with a number of period-doubling cascades, stable periodic-orbit windows and boundary crises. In this plot there are a number of distinct attrac-

tors, uncovered by repeating the scans in C with different initial conditions.

The subsequent panels of figure 11 show iterations of the noisy map drawn as densities on the (C, Δ) –plane for different levels of noise. For $\varepsilon = 10^{-7}$, the density is a slightly smoothed version of the deterministic case (although the noise exposes another unsampled deterministic attractor around $C = 0$ and $\Delta = 15$). Increasing ε up to 10^{-6} further blurs the structure in the density, trun-

cates the doubling cascades at higher periods, and fills in the narrower windows of stable periodic orbits. By $\varepsilon = 10^{-5}$, the densities become much smoother, many of the attractors merge, and larger spacings become infrequent. For the highest noise level ($\varepsilon = 10^{-4}$) the density is much less structured, with no isolated attractors and the remnants of period-doubling cascades disappearing.

VI. CONCLUSIONS

For a large class of nearly homoclinic systems, we have characterized the most significant effect of noise. The main effect is not on the dynamics near to the fixed point, in contrast to the premise of Stone & Holmes³ and others. More significant are stochastic perturbations to the nearly homoclinic transitions away from the fixed point, which critically control where that orbit returns to the neighbourhood of the fixed point, and which in turn dictate the ensuing time of residence. To gauge the true effect of noise, we generalized a singular perturbation analysis of nearly homoclinic pulse trains⁸ to stochastic systems. This furnishes a map that dictates both the pulse spacing and, when the system has reflection symmetry, whether a polarity reversal occurs and a pulse switches to an antipulse or vice versa. The map is a convenient and powerful tool to explore stochastically perturbed homoclinic dynamics and, with a simple change of variable, can be recast into the more conventional form of a one-dimensional map with additive noise. Existing results for such maps can then be immediately carried over to our nearly homoclinic continuous dynamical systems.

Armed with the spacing maps, we explored the impact of noise on the deterministic bifurcation sequences expected near homoclinic connections. In particular, we studied how noise affects the homoclinic explosion of Lorenz flows and the Shilnikov bifurcation sequence. These are the two most commonly encountered scenarios for transition to chaos involving homoclinic orbits. Yet more complex scenarios are possible, however, and one could envision extending our analysis to other situations. For example, much of what we have considered applies to trains of nearly heteroclinic solutions, or noisy front dynamics. Other examples include heteroclinic networks⁷, bifocal homoclinic solutions²⁵ and inverse Shilnikov orbits²⁶. Further afield still, one can envision applying the methodology to analysing the dynamics of coherent structure solutions to stochastically perturbed PDEs (*cf.* Ref. 9).

ACKNOWLEDGMENTS

This work took place during the 2015 Geophysical Fluid Dynamics summer program, Woods Hole Oceanographic Institution, which is supported by the National

Science Foundation and the Office of Naval Research.

- ¹L. P. Shilnikov, "A Contribution To the Problem of the Structure of an Extended Neighborhood of a Rough Equilibrium State of Saddle-Focus Type," *Mathematics of the USSR-Sbornik* **10**, 91–102 (1970).
- ²C. Sparrow, *The Lorenz equations: bifurcations, chaos, and strange attractors*, Vol. 41 (Springer, 2012).
- ³E. Stone and P. Holmes, "Random Perturbations of Heteroclinic Attractors," *SIAM J. Applied Mathematics* **50**, 726–743 (1990).
- ⁴E. Stone and P. Holmes, "Unstable fixed points, heteroclinic cycles and exponential tails in turbulence production," *Physics Letters A* **155**, 29–42 (1991).
- ⁵J. S. Satchell and S. Sarkar, "Stochastic Shilnikov maps," *Journal of Physics A: Mathematical and General* **20**, 1333–1343 (1986).
- ⁶E. Stone and D. Armbruster, "Noise and $O(1)$ amplitude effects on heteroclinic cycles," *Chaos* **9**, 499–506 (1999).
- ⁷D. Armbruster, E. Stone, and V. Kirk, "Noisy heteroclinic networks," *Chaos* **13**, 71 (2003).
- ⁸N. J. Balmforth, G. R. Ierley, and E. A. Spiegel, "Chaotic Pulse Trains," *SIAM J. Applied Mathematics* **54**, 1291–1334 (1994).
- ⁹N. J. Balmforth, "Solitary Waves and Homoclinic Orbits," *Annual Review of Fluid Mechanics* **27**, 335–374 (1995).
- ¹⁰T. Shimizu and N. Morioka, "On the bifurcation of a symmetric limit cycle to an asymmetric one in a simple model," *Physics Letters* **76**, 201–204 (1980).
- ¹¹A. L. Shil'nikov, "On bifurcations of the Lorenz attractor in the Shimizu-Morioka model," *Physica D: Nonlinear Phenomena* **62**, 338–346 (1993).
- ¹²A. Rucklidge, "Chaos in a low-order model of magnetoconvection," *Physica D: Nonlinear Phenomena* **62**, 323–337 (1993).
- ¹³A. Arneodo, P. Coullet, and E. Spiegel, "The dynamics of triple convection," *Geophysical & Astrophysical Fluid Dynamics* **31**, 1–48 (1985).
- ¹⁴J. Hirsch, M. Nauenberg, and D. Scalapino, "Intermittency in the presence of noise: A renormalization group formulation," *Physics Letters A* **87**, 391–393 (1982).
- ¹⁵J. P. Crutchfield, J. D. Farmer, and B. A. Huberman, "Fluctuations and simple chaotic dynamics," *Physics Reports* **92**, 45–82 (1982).
- ¹⁶A. Juel, A. G. Darbyshire, and T. Mullin, "The effect of noise on pitchfork and hopf bifurcations," in *Proceedings of the Royal Society of London A: Mathematical, Physical and Engineering Sciences*, 453 (1997) pp. 2627–2647.
- ¹⁷T. S. Eaves, "Noisy homoclinic pulse dynamics," in *Proceedings, 2015 Geophysical Fluid Dynamics Summer Program*, edited by J. Wettlaufer (Woods Hole Oceanographic Institution, 2015).
- ¹⁸J. Wilkie, "Numerical methods for stochastic differential equations," *Physical Review E* **70**, 017701 (2004).
- ¹⁹N. J. Balmforth and E. A. Spiegel, "Pattern dynamics in a checkerboard map," *Chaos* **14**, 784–792 (2004).
- ²⁰P. Reimann and P. Talkner, "Invariant densities for noisy maps," *Physical Review A* **44**, 6348 (1991).
- ²¹F. T. Arecchi, A. Lapucci, and R. Meucci, "Poincare versus Boltzmann in Shil'nikov phenomena," *Physica D* **62**, 186–191 (1993).
- ²²E. Simiu and M. Frey, "Noise-induced sensitivity to initial conditions," in *Fluctuations and Order: The New Synthesis*, edited by M. Millonas (Springer, 1996) Chap. 6.
- ²³P. Glendinning and C. Sparrow, "Local and global behavior near homoclinic orbits," *J. Statistical Physics* **35**, 645–696 (1984).
- ²⁴P. Glendinning, "Bifurcations near homoclinic orbits with symmetry," *Physics Letters A* **103**, 163–166 (1984).
- ²⁵A. Fowler and C. Sparrow, "Bifocal homoclinic orbits in four dimensions," *Nonlinearity* **4**, 1159 (1991).
- ²⁶P. Glendinning and C. Tresser, "Heteroclinic loops leading to hyperchaos," *Journal de Physique Lettres* **46**, 347–352 (1985).